Plasmoelectric Potentials in Metal Nanostructures

Matthew T. Sheldon,[1] Jorik van de Groep[2],
Ana M. Brown[1], Albert Polman[2], Harry A. Atwater[1]

[1]*Thomas J. Watson Laboratories of Applied Physics, California Institute of Technology, MC 128-95, Pasadena, California 91125, USA*

[2]*Center for Nanophotonics, FOM Institute AMOLF Science Park 104, 1098 XG, Amsterdam, the Netherlands*

† *authors contributed equally*

ABSTRACT

The conversion of optical power to an electrical potential is of general interest for energy applications, and is typically obtained via optical excitation of semiconductor materials. Here, we introduce a new method using an all-metal geometry, based on the plasmon resonance in metal nanostructures. In arrays of Au nanoparticles on an indium-tin-oxide substrate and arrays of 100-nm-diameter holes in 20-nm-thick Au films on a glass substrate, we show negative and positive surface potentials during monochromatic irradiation at wavelengths below or above the plasmon resonance respectively. We observe such plasmo-electric surface potentials as large as 100 mV under 100 mW/cm^2 illumination. Plasmoelectric devices may enable development of entirely new types of all-metal optoelectronic devices that can convert light into electrical energy.

Noble metal nanostructures display remarkable optical properties that arise from the coupling of incident light to the collective motion of the conduction electrons. The excitation, propagation and localization of these plasmons can be tailored by nanoscale control of metal size and shape (*1*). Metal nanostructures exhibiting subwavelength

optical confinement (*2*) have enabled nanoscale photonic waveguides, modulators, enhancement of second harmonic generation, light trapping structures for photovoltaics, and biological labeling techniques (*1*, *2*). Coupling of laser light to plasmonic structures can also result in efficient localized heating, because the resonant absorption cross section for plasmonic nanostructures is much larger than their physical cross section.

Recent work has demonstrated control over the plasmon resonance frequency (ω_p) of metal nanostructures when an external electrostatic field alters the carrier density in the metal (*3*). Increasing the carrier density in a noble metal nanoparticle leads to a blueshift of the resonance, while decreasing it leads to a redshift, as illustrated for a 20-nm-diameter Ag nanoparticle in vacuum (Fig. 1). Interestingly, the reverse effect, the optical generation of an electrostatic potential due to an optically driven change in carrier density in a plasmonic nanostructure has so far not been observed. Thermodynamically, however, such a plasmoelectric effect is expected to occur. We demonstrate direct experimental evidence of plasmoelectric potentials in the range 10-100 mV on colloidal assemblies and plasmonic light harvesting device geometries, in qualitative agreement with a thermodynamic model. The results may provide a new route to convert optical energy into electrical power.

Figure 2A shows the measured scattering spectrum for 60 nm Au colloids on ITO/glass, showing a clear plasmon resonance around λ = 550 nm. Kelvin probe force microscopy (KPFM) (*4*) with a conductive AFM tip in non-contact mode was used to probe the local static potential difference between the tip and sample surface at room temperature (Fig. 2). While the illumination wavelength is gradually scanned through the plasmon resonance spectrum, from 480-650 nm (~1 nm s^{-1}), we probe the potential on the illuminated Au nanoparticle array (S2). A clear optically induced surface potential is observed, that varies with illumination wavelength (Fig. 2B). We observe negative induced potentials during excitation to the blue side of the neutral-particle plasmon resonance wavelength near 550 nm, and positive potentials during excitation on the red side of the resonance, with the measured potential changing sign near the peak of the plasmon resonance.

To model the experimentally observed plasmoelectric effect we consider a metal nanostructure placed on a grounded conducting substrate that is illuminated with monochromatic radiation at a wavelength just below the plasmon resonance λ_p. Random charge fluctuations between particle and substrate will cause the plasmon resonance spectrum to vary by minute amounts (Fig. 1). If an electron is randomly added to the particle, the resonance will blueshift, leading to a concomitant increase in light absorption of the particle, which in turn leads to a small increase in the nanoparticle temperature. The changes in number of electrons *N* and temperature *T(N)* change the free energy *F* of the particle, and an equilibrium charge density is achieved when the free energy is minimum:

$$\frac{\partial F(N,T)}{\partial N} = \left(\frac{\partial F}{\partial N}\right)_T + \left(\frac{\partial F}{\partial T}\right)_N \frac{dT}{dN} = 0 \quad (1)$$

Here, we assume that both the intensity and wavelength of the illumination is constant. Using, by definition, $\left(\frac{\partial F}{\partial N}\right)_T \equiv \mu$, with μ the electrochemical potential, and $-\left(\frac{\partial F}{\partial T}\right)_N \equiv S$, with *S* the entropy of the particle, we find:

$$\mu = S\frac{dT}{dN} \quad (2)$$

Equation 2 shows that under illumination the plasmonic particle adopts a electrochemical potential that is proportional to *dT/dN* . This quantity, which is only determined by the plasmon resonance spectrum and the heat flow from the particle to the substrate, provides the unique thermodynamic driving force in this system. It favors charge transfer to or from the particle that increases absorption, and thereby temperature, in order to lower the free energy. The factor *dT/dN* is largest on the steepest parts of the resonance spectrum; it is positive for irradiation on the blue side of the resonance, leading to a positive chemical potential for the electrons, and hence a negative voltage; the reverse is observed for irradiation on the red side of the resonance. All these trends are exactly as observed in the experimental spectra of Fig. 2B: the surface potential vanishes at the peak of the resonance where *dT/dN* is zero; the largest (negative) potential is

observed at a wavelength of 500 nm, coinciding with the steepest slope in the resonance spectrum of Fig. 2A.

Equation 1 can be used to quantitatively estimate the equilibrium plasmoelectric potential, writing $F(N,T)$ as the sum of the free energies of electrons and phonons, using the well-known free energy functions of an electron and phonon gas (*5, 6*). The electronic term is composed of a contribution due to the chemical potential of the electrons which is directly given by the Fermi function, and an electrostatic contribution due to charging of the metal nanosphere; the phonon term is given by the Debye model. Taking the derivatives to N and T we find analytical expressions for $\mu(N,T)$ and $S(N,T)$, that are then input in Eqn. 2 (S3).

Before applying the model to the experimental geometry in Fig. 2 we calculate the plasmoelectric potential, i.e. the electrochemical potential gained by the particle from the electron transfer induced by optical absorption, for a spherical 20-nm-diameter Ag nanoparticle in vacuum under monochromatic illumination. For these particles analytical Mie theory can be used to calculate the absorption cross section spectrum, $C_{abs}(\lambda, n)$, for a given electron density in the nanoparticle, by taking into account the dependence of the bulk plasma frequency, ω_p, in the complex dielectric function of the metal on carrier density, $\omega_p \propto n^{1/2}$ (S1). To calculate the nanoparticle temperature we use a steady-state heat-flow model in which heat is dissipated from the nanoparticle by radiation. Figure 3A shows the calculated plasmoelectric potential of the Ag nanoparticle as a function of illumination wavelength at an incident flux of 1 mW/cm^2, under which the particle obtains a maximum temperature of ~400 K (S4A). The model predicts a clear negative surface potential below the plasmon resonance and a positive one, up to 150 mV, above it. The asymmetry in the plasmoelectric potential below and above the resonance wavelength is due to the intrinsic non-resonant interband absorption in the metal. Figure 3B shows the corresponding relative absorption increase for the Ag nanoparticle, it ranges up to 2.5×10^{-5}.

The model for the simple geometry in Fig. 3 describes the key factors in the plasmoelectric effect: an increase in carrier density under illumination at wavelengths

shorter than the resonance peak, inducing a negative plasmoelectric potential and enhanced absorption compared with the neutral particle. Similarly, radiation at longer wavelengths induces a lower carrier density, a positive plasmoelectric potential, and enhanced absorption. These results demonstrate that an excited plasmonic resonator behaves as a heat engine that can convert absorbed off-resonant optical power into a static electrochemical potential.

Next, we use the model to calculate the wavelength-dependent and power-dependent plasmoelectric potential for the experimental geometry in Fig. 2, a spherical 60-nm-diameter Au particle on an ITO/glass substrate. We calculated the factor *dT/dN* in Eqn. (2) using Finite-Difference Time-Domain (FDTD) simulations of the absorption spectra for an Au particle on an ITO/glass substrate to take into account radiative damping from the substrate not captured by simple Mie theory and a 1D model for heat conduction into the substrate (S4-5,S8). Due to variations in inter-particle coupling and clustering (see SEM in Fig. 2A), and possible adsorption of water on the particle-ITO interface, the ensemble dielectric environment is complex. The broadened, red-shifted scattering spectrum in Fig. 2A is evidence for some particle aggregation.In the FDTD simulations we model these effects by assuming a background index of $n = 1.4$ for the medium above the ITO substrate, such that the absorption spectrum matches the experimentally observed spectrum. As can be seen in Fig. 2C for the high-power data, the modeled trends correspond well with the experimental trends: the modeled minimum potential occurs at 530 nm (experimental: 500 nm), the modeled zero potential at 545 nm (experimental: 560 nm), and a large positive potential is observed for wavelengths above the resonance, both in model and experiment. The extent of the measured potential to wavelengths up to 640 nm in Fig. 2(b) is in agreement with the long-wavelength tail in the spectrum of Fig. 2(a). At 555 nm the modeled particle temperature peaks at 308 K, 15 K above ambient (S4B), in good agreement with other experimental observations (*7*).

To aid interpretation of our findings, we comment briefly on other mechanisms for generating photopotentials with metals. A thermoelectric effect is several orders of magnitude weaker ($\sim\mu$V ΔK^{-1}) than the observed potentials (*8*). Hot-carrier induced effects would require rectifying contacts which are not present in our geometry.

Moreover, both these effects would not result in a bisignated signal (*9*). "Plasmon drag" or similar direct photon-to-electron momentum transfer mechanisms on Au colloids would not produce a bisignated signal; nor for symmetric hole arrays under normal-incidence irradiation (*10*). Future work will focus on obtaining further insight in the microscopic mechanisms that contribute to the observed effect.

To demonstrate the generality of the observed plasmoelectric effect we measured the plasmoelectric potential on 10-micron-sized arrays of sub-wavelength holes in an optically thin Au film on a glass substrate. In these micro-arrays, light is absorbed by the resonant excitation of interacting surface plasmon polaritons that propagate between the holes on the Au-air and Au-glass interface (*11*) (S9). The absorption spectrum of a single array is determined by the coherent interaction of plasmons within the array, and the study of such arrays thus enables probing the plasmoelectric effect on a single absorber geometry. Moreover, the metal hole array architectures provide a first step towards future plasmoelectric integrated circuitry in which plasmoelectric power is harvested.

Figures 4A,B show a fabricated 10×10-μm hole array composed of 100-nm-diameter holes in a square array with a pitch of 200 nm, made in a 20-nm-thick Au film on a glass substrate. Figure 4C shows the measured absorption spectra of hole arrays with a pitch of 175 – 300 nm (S7). Increasing the pitch leads to a clear redshift in the absorption spectrum. Figure 4D shows the corresponding measured surface potential as a function of the wavelength of illumination (100 mW cm^{-2}), as measured with KPFM. A transition from negative to positive surface potential is seen for each array geometry. Also, the measured potential spectra show a clear redshift with increasing array pitch, in accordance with the trend in the absorption spectra. The maximum plasmoelectric potential observed for each measurement shows a gradually decreasing trend with increasing pitch, also in agreement with the trend in the absorption spectra. A slight difference is observed between the zero-crossing in the potential measurements and the peak in the corresponding absorption spectrum, which is attributed to the difference in numerical aperture (NA) of the microscope objective used for the two measurements (S10). All surface potential spectra show clear minima and maxima and then decrease as the wavelength is tuned further away from the resonance, as expected. The measurements

in Fig. 4D show a plasmoelectric potential as large as ± 100 mV and demonstrate the generality of the plasmoelectric effect for arbitrary plasmonic absorbers.

The observed plasmoelectric phenomenon takes advantage of the remarkable spectral tailorability of plasmonic nanostructures and can be extended to a variety of material systems, absorber geometries, and radiation environments. Plasmoelectric devices may enable development of entirely new types of all-metal optoelectronic devices that can convert light into electrical energy by replacing the usual function of doped semiconductors with metal nanostructures that are optically excited off-resonance.

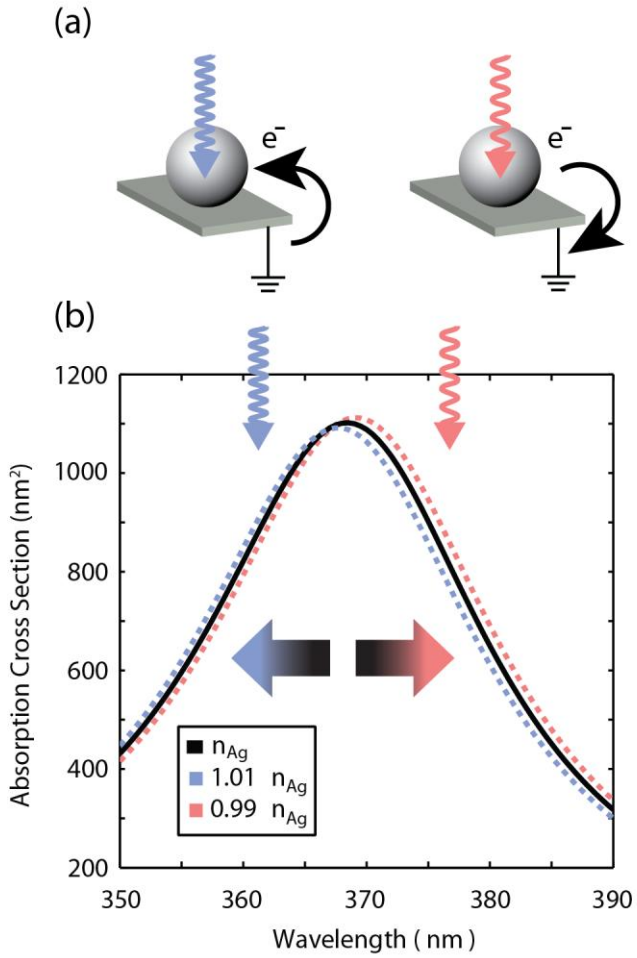

Fig. 1. Absorption cross section spectrum of a Ag nanoparticle and the plasmoelectric effect. Calculated absorption cross section for a 20-nm-diameter Ag nanoparticle in vacuum with bulk carrier density n_{Ag} and carrier densities that are reduced or increased by 1%. Schematics: Spontaneous charge transfer to or from the nanoparticle is thermodynamically favored when the consequent spectral shift increases the absorption, raising the temperature. Irradiation on the blue side of the resonance leads to a negative charge on the particle, irradiation on the red side to a positive charge.

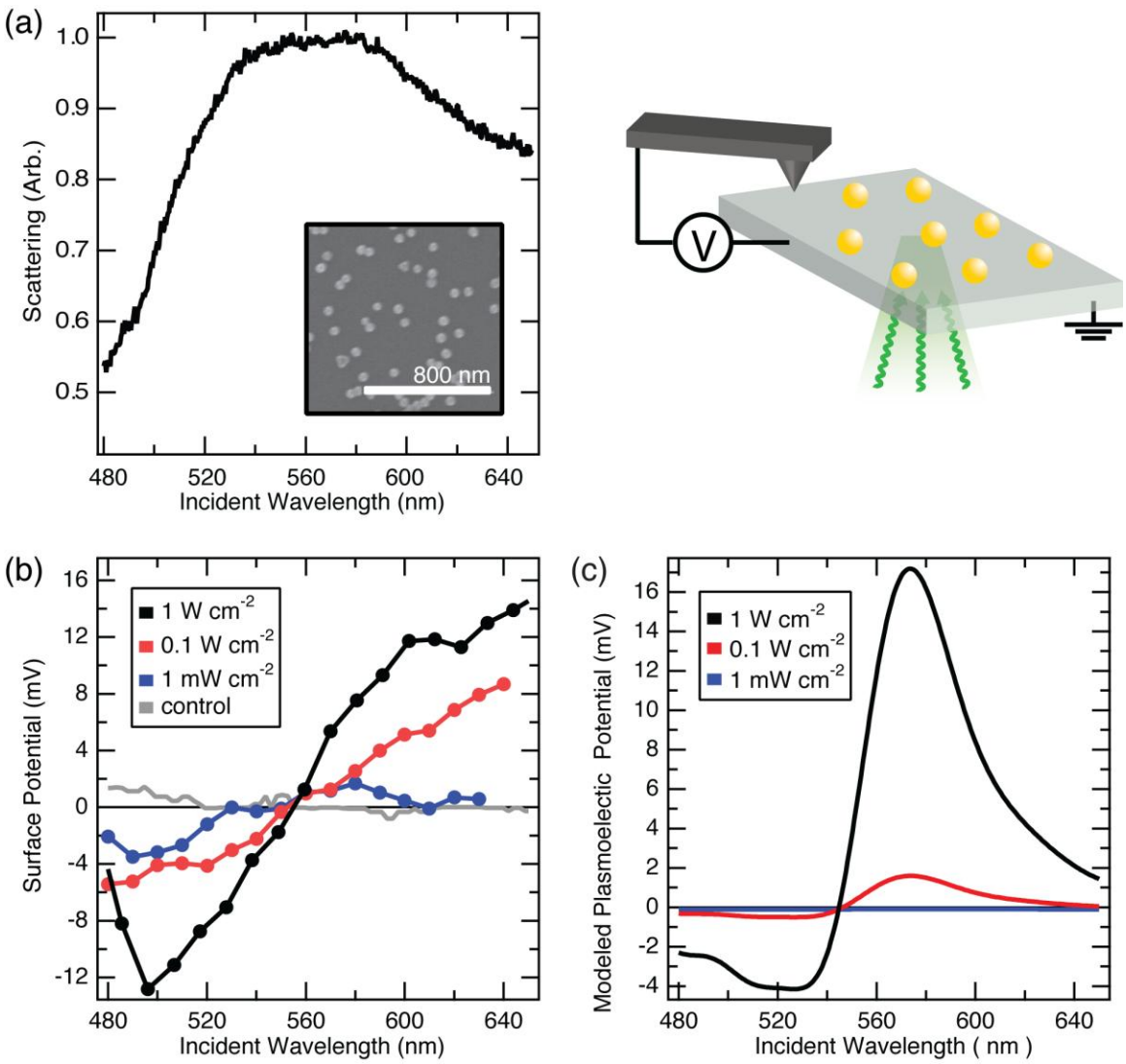

Fig. 2. Plasmoelectric effect on dense Au nanoparticle arrays on ITO/glass. (**A**) Dark-field scattering spectrum of 60-nm-diameter Au nanoparticles on ITO/glass. The inset shows an SEM image of the nanoparticle array. **(B)** Kelvin probe force microscopy measurements of the surface potential as a function of illumination wavelength (15-nm-bandwidth) for three different illumination intensities. The surface potential of a flat region of ITO/glass adjacent to the nanoparticle array was monitored during scanned monochromatic illumination (see schematic geometry). A control measurement of an ITO/glass substrate without nanoparticles (1 W/cm^2) is also plotted (grey). **(C)** Modeled plasmoelectric potential for 60-nm-diameter Au nanoparticles on ITO/glass for the three illumination intensities in (**B**).

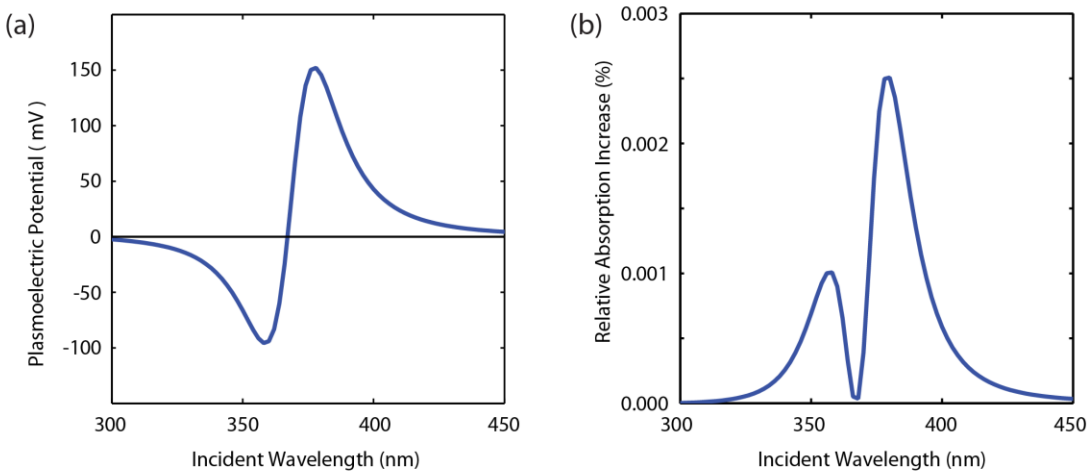

Fig. 3 Modeled plasmoelectric response for Ag nanoparticles. A 20-nm-diameter Ag particle in vacuum is illuminated with monochromatic light (1 mW/cm^2). (A) Plasmoelectric potential and (B) relative absorption increase as a function of incident wavelength.

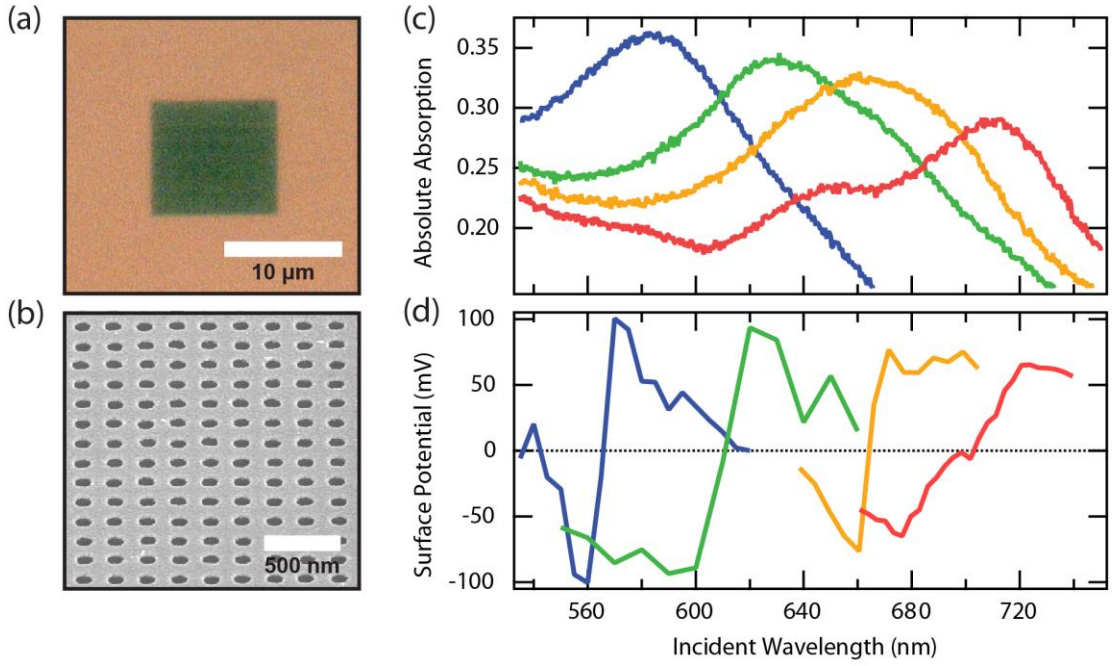

Fig. 4. Plasmoelectric effect on Au nano-hole arrays on glass. (**A**) Bright-field optical microscope image showing a 200-nm-pitch array of 100-nm-diameter holes in a 20-nm-thick Au film on glass. The dark green color directly shows the strong absorption in the hole array. (**B**) SEM image of a 200-nm-pitch hole array imaged under 52 degrees with respect to the normal. (**C**) Measured optical absorption spectra for hole arrays with a pitch of 175 nm (blue), 225 nm (green), 250 nm (yellow) and 300 nm (red) (NA=0.8). (**D**) Surface potential as a function of excitation wavelength measured using Kelvin force probe microscopy at 100 mW/cm^2 for the four hole arrays in (**C**) (NA=0.25).

REFERENCES AND NOTES

1. J. A. Schuller *et al.*, Plasmonics for extreme light concentration and manipulation. *Nat Mater* **9**, 368-368 (2010).
2. L. Novotny, N. van Hulst, Antennas for light. *Nat Photon* **5**, 83-90 (2011).
3. C. Novo, A. M. Funston, A. K. Gooding, P. Mulvaney, Electrochemical charging of single gold nanorods. *Journal of The American Chemical Society* **131**, 14664 (2009).
4. M. Nonnenmacher, M. P. O'Boyle, H. K. Wickramasinghe, Kelvin probe force microscopy. *Applied Physics Letters* **58**, 2921 (1991).
5. N. W. Ashcroft, N. D. Mermin, *Solid State Physics*. (Harcourt, Inc., 1976).
6. B. M. Askerov, S. Figarova, *Thermodynamics, Gibbs Method and Statistical Physics of Electron Gases*. (Springer, New York, 2010).
7. M. G. Cerruti *et al.*, Gold and Silica-Coated Gold Nanoparticles as Thermographic Labels for DNA Detection. *Analytical Chemistry* **78**, 3282-3288 (2006).
8. F. J. Blatt, P. A. Schroeder, C. F. Foiles, *Thermoelectric Power of Metals*. (Plenum Press, New York, 1976).
9. M. W. Knight, H. Sobhani, P. Nordlander, N. J. Halas, Photodetection with active optical antennas. *Science* **332**, 702-704 (2011).
10. N. Noginova, A. V. Yakim, J. Soimo, L. Gu, M. A. Noginov, Phys. Rev. B 84, 035447 (2011) - Light-to-current and current-to-light coupling in plasmonic systems. *Physical Review B*, (2011).
11. W. L. Barnes, W. A. Murray, J. Dintinger, E. Devaux, T. W. Ebbesen, Surface Plasmon Polaritons and Their Role in the Enhanced Transmission of Light through Periodic Arrays of Subwavelength Holes in a Metal Film. *Physical Review Letters* **92**, 107401 (2004).
12. E. D. Palik, *Handbook of Optical Constants of Solids*. (Academic, New York, 1985).
13. A. Rakic, A. Djurisic, J. Elazar, M. Majewski, Optical properties of metallic films for vertical-cavity optoelectronic devices. *Appl Optics* **37**, 5271-5283 (1998).
14. G. V. Hartland, Optical studies of dynamics in noble metal nanostructures. *Chemical Reviews* **111**, 3858-3887 (2011).
15. S. A. Maier, *Plasmonics: Fundamentals and Applications*. (Springer, New York, 2007).
16. J. M. Luther, P. K. Jain, T. Ewers, A. P. Alivisatos, Localized surface plasmon resonances arising from free carriers in doped quantum dots. *Nature Materials* **10**, 361-366 (2011).
17. G. Garcia *et al.*, Dynamically modulating the surface plasmon resonance of doped semiconductor nanocrystals. *Nano Letters* **11**, 4415-4420 (2011).
18. J. Gordon, S. Ernst, Surface-plasmons as a probe of the electrochemcial interface. *Surf Sci* **101**, 499-506 (1980).
19. K. F. Macdonald, Z. L. Sámson, M. I. Stockman, N. I. Zheludev, Ultrafast active plasmonics. *Nature Photonics* **3**, 55-58 (2009).
20. V. Palermo, M. Palma, P. Samorì, Electronic Characterization of Organic Thin Films by Kelvin Probe Force Microscopy. *Advanced Materials* **18**, 145-164 (2006).
21. W. Shockley, H. J. Queisser, Detailed balance limit of efficiency of p‐n junction solar cells. *Journal Of Applied Physics* **32**, 510-519 (1961).
22. C. Kittel, *Introduction to Solid State Physics*. (Wiley, New York, ed. 8th, 2005).
23. P. T. Landsberg, G. Tonge, Thermodynamic energy conversion efficiencies. *Journal of Applied Physics* **51**, R1-R20 (1980).
24. J. P. Holman, *Heat Transfer*. (McGraw-Hill, ed. 10th, 2009).
25. N. D. Lang, W. Kohn, Theory of metal surfaces: induced surface charge and image potential. *Physical Review B* **7**, 3541 (1973).

26. T. Sannomiya, H. Dermutz, C. Hafner, J. Vörös, A. B. Dahlin, Electrochemistry on a localized surface plasmon resonance sensor. *Langmuir* **26**, 7619-7626 (2010).
27. P. B. Johnson, R. W. Christy, Optical Constants of the Noble Metals. *Physical Review B* **6**, 4370-4379 (1972).
28. B. Luk'yanchuk *et al.*, The Fano resonance in plasmonic nanostructures and metamaterials. *Nat Mater* **9**, 707-715 (2010).
29. L. S. Inc.
30. J. Parsons *et al.*, Localized surface-plasmon resonances in periodic nondiffracting metallic nanoparticle and nanohole arrays. *Physical Review B* **79**, 073412 (2009).
31. J. Braun, B. Gompf, G. Kobiela, M. Dressel, How Holes Can Obscure the View: Suppressed Transmission through an Ultrathin Metal Film by a Subwavelength Hole Array. *Physical Review Letters* **103**, 203901 (2009).
32. R. W. Alexander, G. S. Kovener, R. J. Bell, Dispersion Curves for Surface Electromagnetic Waves with Damping. *Physical Review Letters* **32**, 154-157 (1974).
33. G. S. Kovener, R. W. Alexander, Jr., R. J. Bell, Surface electromagnetic waves with damping. I. Isotropic media. *Physical Review B* **14**, 1458-1464 (1976).
34. A. F. Koenderink, A. Polman, Complex response and polariton-like dispersion splitting in periodic metal nanoparticle chains. *Physical Review B* **74**, 033402 (2006).
35. T. W. Ebbesen, H. J. Lezec, H. F. Ghaemi, T. Thio, P. A. Wolff, Extraordinary optical transmission through sub-wavelength hole arrays. *Nature* **391**, 667-669 (1998).

ACKNOWLEDGEMENTS

The authors gratefully acknowledge support from the Department of Energy, Office of Science under grant DE-FG02-07ER46405 (MS and HAA) and for facilities of the DOE "Light-Material Interactions in Energy Conversion" Energy Frontier Research Center (DE-SC0001293). Work at AMOLF is part of the research program of the Foundation for Fundamental Research on Matter, which is financially supported by the Netherlands Organization for Scientific Research (NWO). It is also supported by the European Research Counsel. One of us (AB) acknowledges support from an NSF Graduate Research Fellowship. The data are archived in the laboratory of HAA. Helpful discussions with E. Kosten, V. Brar, D. Callahan, M. Deceglie, A. Leenheer, J. Fakonas, R. van Roij and H.J. Bakker are gratefully acknowledged.

SUPPLEMENTARY MATERIALS

Materials and Methods

Supplementary Text

Figs. S1 to S9

References (12 – 35)

Supplementary Materials for

Plasmoelectric Potentials in Metal Nanostructures

Matthew T. Sheldon, Jorik van de Groep, Ana M. Brown, Albert Polman, Harry A. Atwater

correspondence to: haa@caltech.edu

This PDF file includes:

Materials and Methods
Supplementary Text
Figs. S1 to S9
References (12 – 35)

Materials and Methods

Colloid Materials and Preparation:

60-nm-diameter Au colloids (BBI International, EM.GC60 Batch #15269, OD1.2) were used for optical and electrical measurements. Samples for electrical characterization were prepared on indium tin oxide (ITO) coated glass substrates (SPI brand, 30-60 Ω, 06430, ITO layer thickness: 100 nm) that were first ultrasonicated overnight in a solution containing an equal volume of acetone, methanol, toluene, and isopropyl alcohol and then dried with N_2. Substrates were placed individually in glass scintillation vials (ITO-side up) with 600 µL Au colloid diluted by 1.2 mL of deionized (DI) water; for control samples, DI water was used instead of the Au colloid solution. Then 60 µL 0.1 M HCl was added, and the vials were immediately centrifuged at 2000 rpm (~670 g-force) for 40 minutes. After centrifuging, the solution had become clear and the ITO film had a noticeable red color due to Au nanoparticles deposited on the surface. Subsequently, the substrates were rinsed thoroughly with DI water and heated to 290 °C by placing a heat gun 5 cm above the sample surface for 20 minutes. The scattering spectra of the deposited samples (as in Fig. 2A) were obtained using a Zeiss Axio Observer inverted microscope equipped with a 20× dark-field objective, with illumination from a halogen lamp.

Hole Array Fabrication

10×10 micron sized hole arrays in 20 nm thick Au, with 100 nm hole diameter and pitch in the range of 150-300 nm, were fabricated on 1-mm-thick glass using electron-beam lithography. A three-layer process was used to fabricate a shadow mask for Au evaporation. First, 240 nm PMMA 35k300 was spincast on a clean glass substrate, and baked at 180 °C for 15 min. Next, 25 nm of Ge was thermally evaporated (0.5 Å/s) to make the substrate conductive and to protect the PMMA during further processing. Finally, 65 nm of hydrogen silsesquioxane (HSQ) negative tone resist (2 MIBK : 1 Fox 15 dilution) was spincoated and baked at 180 °C for 2 min. Proximity-corrected square arrays of disks were written in the HSQ (20 kV, 7.5 µm aperture, 10.7 pA beam current) using area exposure with a dose of 200-500 pAs/cm^2 (depending on pitch). The HSQ was developed by submerging in MF-319 (Microposit developer) at 50 °C for 60 s, followed by thorough rinsing with d$H_2$0. The disk patterns were transferred into the PMMA by subsequent anisotropic reactive-ion etching of the Ge (using SF_6 and O_2) and PMMA (using O_2). Next, 20±2 nm of Au was thermally evaporated at 0.5 Å/s. Finally, lift-off was performed by dissolving the PMMA in acetone at 50 °C for 3 hours, followed by 10 min of megasonification and 1 min of ultrasonification, both in acetone.

Hole Array Optical Characterization

Transmission and reflection spectra of the hole arrays were measured using a WiTec-α optical microscope. A fiber-coupled white light source (Ando AQ-4303B) in combination with a 9 µm-core fiber was used to illuminate the hole arrays through a 60× objective (Nikon, NA=0.8, WD=0.3 mm), resulting in a 3-4 µm diameter spot (unpolarized). The transmission was collected by a 50× objective (Nikon, CFI L-Plan EPI CR, NA=0.7, WD=3 mm corrected for substrate thickness). Both the transmitted and reflected light was coupled into a 100-µm-core collection fiber and analyzed by a spectrograph (Acton 300i) and Si CCD, which was cooled to -45 °C (Roper Scientific,

model 7344-0001). Each spectrum is an average of 100 frames with 250 ms accumulation time each.

Supplementary Text

S1. Complex Dielectric Function of Ag and Au

To calculate the absorption cross section spectra of a Ag nanoparticle (Fig.1), we apply a 6th-order, multiple oscillator Lorenz-Drude model of the complex dielectric function of silver, fit to data from Palik (*12*). For the dielectric function of Au we use a Brendel–Bormann Gaussian oscillator model. We use the method outlined by Rakic and coworkers (*13*). These dielectric functions accurately reproduce the observed extinction spectra of spherical silver or gold nanoparticles when input into the exact analytic solutions to Maxwell's equations provided by Mie theory (*14*). To introduce the explicit dependence on electron density, n, we assume that all terms in the dielectric function that depend on the bulk plasma frequency, ω_p^* , depend on electron density, n, according to a simple Drude model relation,

$$\omega_p^* = \left(\frac{n \cdot e^2}{\varepsilon_o \cdot m_e^*} \right)^{1/2} \qquad (S1)$$

where e is the electron charge, ε_o is the permittivity of free space, and m_e^* is the electron effective mass (*15*). This strategy is consistent with other work that examined carrier density-dependent plasmon shifts, for example in doped semiconductors, electrochemical cells, or at metal surfaces during ultrafast pump-probe measurements (*16*-*19*). Figure S1 shows the calculated relative change of the absorption cross section of a 20-nm-diameter Ag nanoparticle in vacuum, as a function of wavelength and electron density, n, compared with the absorption cross section for a neutral Ag silver particle with electron density n_{Ag}.

S2. Kelvin Probe Force Microscopy (KPFM) of Au Colloids on ITO/glass and Au Hole Arrays

For KPFM characterization of colloid particles on ITO/glass, the sample was measured at the limit of highest possible particle coverage, and it was anticipated that the measured region of ITO/glass adjacent to the Au particles was equipotential with the particles. Direct illumination of the AFM tip was avoided, and there was no dependence of the magnitude of signal based on the distance from the optical spot, within ~10's of μm. A control measurement of ITO/glass free of Au colloids is shown in Fig S2 and shows no detectable wavelength-dependent signal. The absolute surface potential determined by the KPFM technique is always a convolution of the work function difference between the sample and a particular tip, and factors relating to the tip-sample geometry that define capacitance. Therefore, to emphasize wavelength-dependent changes of potential, the reported data (Fig. 2B) are plotted relative to the surface potential in the same spot measured in the dark before optical excitation.

For KPFM measurements of hole arrays, an optical spot encompassing the entire array was incident directly beneath the AFM tip. The plotted data (Fig. 4D) are the average response of the entire 10×10 μm array integrated over ~20 min with a single wavelength incident. This procedure allowed the sample to stabilize from any drift during

the course of the measurement, and, by measuring a structure much larger than the tip, maximized the accuracy of the KPFM technique (*20*). Because the tip was illuminated, even control measurements of smooth Au films detected uniform changes in the KPFM signal based on whether the tip was illuminated or in the dark. This signal results from optical heating of the tip, while other contributions to the measured potential, such as photo-carrier generation in the tip, may also be manifest. The magnitude of the light vs. dark response, though independent of incident wavelength, was dependent on the incident power as well as the particular tip used. Therefore we could not employ the same simple subtraction procedure used to offset the data during the colloid measurements on ITO, as described above.

However, relative changes in the surface potential of the hole arrays that were dependent on the wavelength of illumination were stable and reproducible, and were independent of the tip employed or the tip distance from the sample, over a range of tip distances spanning ~ 1 to 100 nm. For this reason, the curves from different arrays in Fig. 3D are plotted to emphasize the comparison between wavelength-dependent changes, with zero set by the mid-point of the maximum and minimum surface potential measured from that array.

S3. Thermodynamic model for calculating plasmoelectric potentials

(A) Introduction

Our thermodynamic model posits that there is a well-defined, constant temperature, T, of a plasmonic nanoparticle during steady-state illumination at a single wavelength, λ, and intensity, I_λ. This constant T results from the requirement that the optical power absorbed and thermal power conducted away or radiated by the nanoparticle must be equivalent in a steady state. This temperature is a function of the absorption cross section, C_{abs}, of the nanostructure, which also depends on the electron density, n, due to the strong dependence on n in the complex dielectric function of the metal. Then, $T(n, \lambda)$ is the unique thermodynamic function of state that distinguishes an illuminated plasmonic absorber from one in the dark.

We assert that it is reasonable to define such a temperature for a resonantly heated particle, because electronic relaxation processes are fast and the electronic system and lattice are in equilibrium. We note that similar arguments are central to, for example, the detailed balance calculation of the limiting efficiency of a photovoltaic cell (*21*). This well-defined temperature describes a local thermal equilibrium in a thermodynamic system enclosing the particle, and motivates a thermodynamic equilibrium argument based on free energy minimization.

(B) Free Energy Minimization

We consider a nanoparticle under steady-state, monochromatic illumination at a wavelength near the plasmon resonance. The electron density of the particle can change via charge transfer through an electrical connection to a DC electrical conductor assumed to have no plasmonic response. We solve for the configuration of the nanoparticle where the free energy, F, of the particle is minimized with respect to free electron density, n, for a given irradiation wavelength λ and power density I_λ. That is, where

$$\frac{dF}{dn} = 0 \quad . \qquad (S2)$$

For convenience, we convert between electron density, n, and the total number of unbound electrons in the particle, N, with the relation $N = nV$, where V is the (constant) volume of the nanoparticle. The total free energy of the nanoparticle, F_{tot}, is a function of N and temperature, T, the latter also depending on N and as outlined above. The differential quantity can be expanded:

$$\frac{\partial F_{tot}(N,T)}{\partial N} = \left(\frac{\partial F_{tot}(N,T)}{\partial N}\right)_T + \left(\frac{\partial F_{tot}(N,T)}{\partial T}\right)_N \frac{dT(N)}{dN} = 0 \quad (S3)$$

where the subscripts T or N indicate that that variable is held constant in the derivative. Note that both the intensity and wavelength are assumed to be constant, and are therefore not included in the partial derivative for simplicity. The electrochemical potential of the particle, μ, is by definition the quantity

$$\left(\frac{\partial F_{tot}(N,T)}{\partial N}\right)_T \equiv \mu(N,T) \quad . \qquad (S4)$$

Additionally, the entropy of the particle, S, is by definition

$$-\left(\frac{\partial F_{tot}(N,T)}{\partial T}\right)_N \equiv S(N,T) \quad . \qquad (S5)$$

Then, the free energy minimum corresponds to a configuration with a number of electrons, N, such that

$$\mu(N,T) = S(N,T)\frac{dT(N)}{dN} \quad . \qquad (S6)$$

Expression $(S6)$ is the central insight that predicts the plasmoelectric effect. It shows that an illuminated plasmonic particle adopts a non-zero electrochemical potential that is proportional to $dT(N)/dN$. The sign and magnitude of this potential is determined by how changes of charge density modify the absorption cross section, and hence the temperature of the nanoparticle, for the given incident wavelength.

(C) Calculation for the Configuration of Minimum Total Free Energy, $\boldsymbol{F_{tot}}$

We determine the total free energy, F_{tot}, of the nanoparticle by considering the separate contributions from the electrons, F_e, and the phonons, F_p:

$$F_{tot}\big(N,T(N)\big) = F_e\big(N,T(N)\big) + F_p\big(T(N)\big) \quad . \qquad (S7)$$

Note that for the optical power densities we consider, because of the fast electronic relaxation rate and electron-phonon coupling rate in a metal, the electron temperature and phonon temperature are equivalent (*14*):

$$T_{electron} \approx T_{phonon} = T(N) \quad . \quad (S8)$$

F_e is defined in terms of the chemical potential of the electrons, μ_e, and the electrostatic potential on the particle, ϕ, as

$$F_e\big(N, T(N)\big) = \int_0^N \mu_e\big(N', T(N')\big)dN' + \int_0^{N-N_o} \phi(N' - N_o)dN' \qquad (S9)$$

where N_o is the number unbound electrons on the neutral particle, and μ_e equals the Fermi function with a small (< 0.1%) temperature correction (5)

$$\mu_e\big(N, V, T(N, \lambda)\big) = \epsilon_F(N, V)\left(1 - \frac{1}{3}\left(\frac{\pi k_b T(N, \lambda)}{2\epsilon_F(N, V)}\right)^2\right) \qquad (S10)$$

with

$$\epsilon_F(N, V) = \frac{\hbar}{2m}\left(\frac{3\pi^2 N}{V}\right)^{2/3} \quad , \qquad (S11)$$

and ϕ is the electrostatic potential for a conducting sphere:

$$\phi(N - N_0) = \frac{e^2(N - N_0)}{4\pi R\varepsilon_0\varepsilon_m} \qquad (S12)$$

with R the sphere radius, e the electron charge and ε_0 and ε_m the permittivity of free space and the relative permittivity of the surrounding medium, respectively.

F_p is defined in terms of the speed of sound in the particle, v_s, via the Debye temperature, θ, with (*6*, *22*)

$$F_p\big(T(N)\big) = 3k_b T(N)A_0 ln\left(\frac{\theta}{T(N)}\right) - k_b T(N)A_0 \qquad (S13)$$

and

$$\theta = \frac{\hbar v_s}{k_b}\left(\frac{6\pi^2 A_0}{V}\right)^{1/3} \qquad (S14)$$

where k_b is Boltzmann's constant, and A_0 the number of atoms in the particle which here is equal to N_o. For Au, $\theta \approx 170\ K$ (*5*). Expression $(S14)$ is the high-temperature limit of the quantum Debye model, valid for $T > \theta$.

The total electrochemical potential μ and the entropy *S* can now be derived by applying Eqs. $(S4)$ and $(S5)$, respectively, to expression (*S7*) for the free energy. We find

$$\mu\big(N, T(N)\big) = \epsilon_F(N, V) - \frac{m{k_b}^2 T(N)^2}{6\hbar^2}\left(\frac{\pi V}{3N}\right)^{2/3} + \frac{e^2(N - N_0)}{4\pi R\varepsilon_0\varepsilon_m} \qquad (S15)$$

and

$$S\big(N, T(N)\big) = \int_0^N \frac{1}{3}\frac{\pi^2 {k_b}^2 T(N')}{2\epsilon_F(N')}dN' - 3k_b A_0 ln\left(\frac{\theta}{T(N)}\right) + 4k_b A_0 \quad . \qquad (S16)$$

The steady-state charge configuration (value of *N*) that corresponds to the minimum free energy can then be obtained by using eqs. $(S15)$ and $(S16)$ to solve Eq. $(S6)$. This leads to

$$\epsilon_F(N) - \frac{m{k_b}^2 T(N)^2}{6\hbar^2}\left(\frac{\pi V}{3N}\right)^{\frac{2}{3}} + \frac{e^2(N - N_0)}{4\pi R\varepsilon_0\varepsilon_m} - \int_0^N \frac{1}{3}\frac{\pi^2 {k_b}^2 T(N')}{2\epsilon_F(N')}dN'\frac{dT(N)}{dN} + 3k_b A_0 ln\left(\frac{\theta}{T(N)}\right)\frac{dT(N)}{dN} - 4k_b A_0\frac{dT(N)}{dN} = 0\,. \qquad (S17)$$

This equation can be solved to find the steady-state value for N (for given λ and I_λ) using as input the function $dT(N)/dN$ which is determined by the plasmon resonance spectrum and the heat conducted or radiated away from the particle.

(D) Theoretical efficiency limit

This thermodynamics model shows that an excited plasmonic resonator behaves as a heat engine that can convert absorbed off-resonant optical power into a static electrochemical potential. In principle, optical-to-electrical energy conversion by this mechanism could be optimized to perform with an efficiency at the Carnot limit, as with any generalized heat engine (*23*).

S4. Temperature Calculations

(A) Ag nanoparticle in vacuum

To calculate the plasmoelectric potential for a Ag nanoparticle in vacuum we calculate the temperature of the nanoparticle, T, given the absorption cross section $C_{abs}(n, \lambda)$ from S1 and incident power density. Under steady state illumination, the power absorbed by the particle must equal the power going out:

$$P_{in} = P_{out} \quad . \quad (S18)$$

P_{in} constitutes the absorbed monochromatic optical radiation plus the absorbed thermal radiation from the ambient background (at $T_{amb} = 293$ K).

$$P_{in} = C_{abs}(n,\lambda)I_\lambda + \sigma A\varepsilon {T_{amb}}^4 \quad . \quad (S19)$$

Here, σ is the Stefan Boltzmann constant, A is the surface area of the nanoparticle, and ε is the emissivity. The nanoparticle emissivity $\varepsilon = 0.01$ was experimentally determined using FTIR absorption spectroscopy on gold colloids, assuming reciprocity of the absorption and emission in the 2-5 μm wavelength range of the measurement. This value is close to that of bulk gold and silver in the infrared, as reported elsewhere (*7*) and predicted by Mie theory. For Ag nanoparticles in vacuum the only loss channel for the power is thermal radiation, defining

$$P_{out} = \sigma A\varepsilon T^4 \quad . \quad (S20)$$

Solving eq. $(S18)$ for the temperature of the particle then gives

$$T(n,\lambda) = \left(\frac{C_{abs}(n,\lambda)I_\lambda + \sigma A\varepsilon {T_{amb}}^4}{\sigma A\varepsilon}\right)^{1/4} \quad . \quad (S21)$$

Figure S3 shows the calculated temperature for a 20-nm-diameter Ag nanoparticle in vacuum as a function of illumination wavelength for an incident power densities of 1 mW/cm^2; it peaks at 400 K. The calculated temperature and its dependence on *N*, *dT(N)/dN* (for a given λ and I_λ) are then used as input in solving Eqn. (*S*17) for the case of a Ag nanoparticle in vacuum (see S5).

(B) Au nanoparticles on ITO

To calculate the temperature of Au nanoparticles on ITO/glass we first calculate the absorption cross section spectrum $C_{abs}(n,\lambda)$ using finite-difference-time-domain (FDTD) full wave electromagnetic simulations. In the experiment, the exact dielectric surrounding of the nanoparticle is very complex. As shown in Fig. 2A, there are large variations in inter-particle spacing as well as clusters with different configurations, both inducing near-field coupling and thereby red-shifted resonance wavelengths. Furthermore, the KPFM experiments were performed in ambient conditions, such that adsorption of water to the particle-ITO interface is likely. Since the exact influence of such conditions on the plasmoelectric potential is beyond the scope of this paper, we simplified the geometry to a single 60 nm Au nanoparticle on an ITO substrate. We assumed a uniform background index of $n = 1.4$ to take into account the red-shift due to the dielectric surrounding described above, such that the modeled scattering spectrum represented the measured scattering spectrum. We then calculate the steady-state power balance to obtain the nanoparticle temperature. Heat flow into the substrate is modeled using a 1D heat transfer model, as sketched in Fig. S4, with the particle on a glass substrate with thickness d = 1 mm covered by a thin layer of ITO. We use the thermal heat conductivity for glass of $\sigma_T = 1.05$ W m^{-1}K^{-1} (*24*). The heat of the particle can be transferred from the particle (at T_{part}) through a cylinder of glass with cross sectional area equal to the contact area $A_{contact}$ between the glass and the particle, to the bottom of the substrate (at ambient temperature, T_{amb} = 293 K). The heat flow is given by (*24*)

$$P_{diff} = \sigma_T \frac{(T_{part} - T_{amb})}{d} A_{contact} \qquad (S22)$$

Figure S4 shows the calculated temperature of the Au nanoparticle as a function of incident wavelength for the three different intensities used in Fig. 2B. In these calculations the parameter $A_{contact}$ is tuned such that the calculations of the surface potential (see S5) best match the experimentally observed surface potential for the largest power densities. The best fit for the contact area is 2.5 times the geometrical particle cross section, a reasonable value given the simple heat flow model. The same contact area is then used for the lower power densities to calculate the temperature profiles in Fig. S4 and the surface potentials in Fig. 2C. We find the same power-dependent trend for slightly more complicated 2D and 3D heat diffusion models, with the assumed contact area between the particle and ITO dominating the magnitude of the temperature. The maximum temperature calculated in Fig. S4 amounts to 308 K, 15 degrees above ambient temperature, which is a reasonable temperature to sustain for an Au nanoparticle on a substrate. Note that the increase of temperature due to the plasmoelectric effect compared with a neutral particle is only of order of up to 10s of mK, depending on geometry and illumination intensity. The calculated temperature and its dependence on N, *dT(N)/dN* (for a given λ and I_λ) are used as input in solving Eqn. (*S*17) for the case of Au nanoparticles on ITO/glass (see S5).

S5. Calculation of Steady-State Nanoparticle Surface Potential and Charge

Using the temperature and values for $dT(N)/dN$ described in S4 we solve Eqn. (*S*17) to determine the steady-state surface potential and corresponding charge on the nanoparticle as a function of irradiation wavelength. Figure S5 shows the calculated charge density $N\text{-}N_0$ for Au nanoparticles on ITO/glass, for the highest experimental power density of Fig. 2B (I_λ=1000 mW/cm^2). The calculations use 6.67x10^6 Au atoms for a 60-nm-Au sphere. As can be seen, the excess electron number $N\text{-}N_0$ is modulated around a value of $N\text{-}N_0$ = -104.69 electrons, observed at the peak of the resonance (no plasmoelectric effect, dN/dT=0). This corresponds to the number of electrons for which the total electrostatic charging energy equals the Fermi energy for Au E_F=5.02 eV. In the dark, the offset between the Fermi level of the particle and the substrate will induce a compensating electrostatic charge on the particle, which is the usual condition for electrochemical equilibration between two dissimilar conductors. Note that the presence of the ITO substrate can be easily accounted for by subtracting the Fermi energy of the ITO substrate, such that the offset observed in Fig. S5 is in fact the difference in Fermi energy between the particle and the ITO. Correcting for this "dark" charge (right-hand scale in Fig. S5) we see that in the time-averaged situation, less than one electron on average is added or removed from the nanoparticle to generate the observed plasmoelectric potential. The data in Fig. S5 can be converted to surface potential, as shown in Fig. 2C. Additionally, we note that the thermoelectric effect (omitted in our analysis) induces only a minor contribution to the potential state of the particle, even for large temperature gradients between the substrate and particle, because of the small Seebeck coefficient of metals, $\sim \mu$V/ ΔK (*8*).

S6. Charge Accumulation Shell Model

The calculations described above assume that any additional charge carriers that are transferred to the particle are uniformly distributed throughout the nanoparticle. However, electrostatic models require that any surplus charges reside on the surface of a metal object (less than 1 nm thickness), since no static electric fields can exist inside the metal (*25*). On the other hand, the surface plasmon resonance is a dynamic phenomenon, with electromagnetic fields that penetrate into the metal as defined by the electromagnetic skin-depth, which is ~3-10 nm for Ag and Au at optical frequencies, and an electron mean free path that is larger than the Fermi screening length. Additionally, the plasmon resonance frequency is predominately determined by the electron density of the very outer layer within the optical skin depth of the metal, as reported experimentally (*26*) and verified by us using FDTD simulations. Therefore, electrostatic arguments suggest that any additional charges will reside near the surface of the nanoparticle, and electrodynamic arguments suggest that only the electron density near the outer surface needs to be increased in order to blue-shift the plasmon resonance. If excess charge resides only near the surface, the plasmoelectric effect thus requires a smaller number of electrons to obtain the same frequency shift, and thereby $dT(N)/dN$ in eq. $(S6)$ is larger.

To study the influence of non-uniform distributions of charge density in the particle, we consider a simplified shell model, in which we assume that all the additional charge carriers transferred due to the plasmoelectric effect reside in the outer shell with thickness δ (see inset of Fig. S6). To implement the shell in eq. $(S17)$, one has to express the Fermi energy, temperature, and N and V in terms of the number of electrons in the shell and the shell volume rather than the whole particle. Eq. $(S17)$ can then be solved for the number of electrons in the shell, assuming a certain shell thickness.

Figure S6 shows the plasmoelectric potential (a) and the relative increase in absorption (b) for a 20-nm-diameter Ag particle in vacuum, as a function of illumination wavelength ($10\ \mathrm{mW/cm^2}$), for different shell thicknesses. Figures S6 A and B clearly show the effect of a thinner shell: the transferred electrons induce a relatively larger increase in electron density and thereby a larger increase in absorption (Fig. S6 B). Note that for shell thicknesses larger than 1 nm, the magnitude of the potential rapidly converges to that obtained with uniform charge distribution ($\delta = 10$ nm, green curves). Uniform charge distribution is assumed for calculations throughout this manuscript. Further arguments for assuming a uniform distribution of charge include the fact that the area under the absorption spectrum of a dipolar plasmon mode should only scale with the total number of valence electrons in the metal, irrespective of their location inside the particle.

S7. Transmission and Reflection Experiments on Hole Arrays

The absorption spectra for the hole arrays in Au in Fig. 4 are derived from transmission and reflection spectra measured in an optical microscope. Light from a broadband light source (Ando AQ-4303B) was focused onto the 10×10 μm hole arrays to a ~4 μm diameter spot using a 0.8 NA microscope objective. Transmitted and reflected light intensities were recorded using a fiber-coupled spectrometer equipped with a Si CCD array detector. To calibrate the measured transmitted and reflected intensity spectra, the transmission spectrum was measured for a bare region of the gold film, next to the hole arrays, and normalized this to the measured transmission of bare glass. Figure S7A

shows the resulting transmission spectrum for the bare Au film (dark blue). For comparison, the transmission obtained from Fresnel calculations of a air-Au-glass layer system (light blue) is shown, assuming a Au layer thickness of 18 nm and optical constants from Johnson and Christy (*27*). The calculated transmission was multiplied by a factor 0.96 to correct for the 4% reflection on the bottom interface in the experimental geometry. Figure S7A shows very good agreement between the measured and calculated spectra which provides further confidence in the normalization procedure for the transmission measurements.

Reflection measurements were normalized using the calculated reflection spectrum for the bare gold film, which is shown in Figure S7B, as a reference. This procedure does not take into account the small reflection from the bottom interface of the glass substrate. Therefore, derived reflectivities are slightly overestimated. The accuracy of all derived transmittance and reflectance spectra is within 5%.

Figure S7C,D shows measured transmission and reflection spectra for all hole arrays, with pitch ranging from 150 nm to 300 nm in steps of 25 nm. A clear dip is observed both in transmission and reflection spectra resulting from the resonant absorption in the hole array. The dips show a clear redshift with increasing pitch, as expected. The wavelength of the dip in transmission is significantly blueshifted with respect to the dip in reflection, which is due to interference between directly transmitted light and forward scattered light (Fano-effect) (*28*).

The absorption spectra for the hole arrays in Fig. 4C were calculated from the measured spectra as $Abs = 1 - R - T$. This analysis slightly overestimates the actual absorption, as it neglects the small amount of light scattered in angles beyond the NA of the collection aperture. However, this fraction will be small, since no diffraction orders can occur in the visible spectral range for the used array pitch.

S8. FDTD Simulation Details

We performed full wave modeling using Lumerical finite-difference time-domain (FDTD) (*29*) simulations to determine the scattering and absorption spectra for Au particles on ITO and to simulate the transmission and reflection spectra for Au hole arrays. Optical constants for Au are as described in S1, taken from Johnson and Christy (*27*) for Fig. S7, and using the Brendel and Bohrmann model (*13*) for all other calculations. For ITO they were taken from spectroscopic ellipsometry measurements of sputtered ITO films.

For simulations of Au colloids on ITO, we modeled a 60-nm-diameter Au sphere on top of an ITO slab and a background index of $n = 1.4$ (see S4B). The simulations employed Perfectly Matching Layer (PML) boundary conditions on all boundaries. We used a Total Field Scattered Field (TFSF) source to launch and extinguish broadband plane waves (λ =460–650 nm). The scattering and transmission due to the sphere were recorded and used to calculate the absorption and extinction spectra.

For the hole array geometry, we modeled a 20-nm-thin Au film on top of a glass substrate (index n = 1.46), and applied PML boundary conditions at the top and bottom interfaces of the simulation box to mimic semi-infinite media for both the glass substrate and air. A 100-nm-diameter hole is positioned in the center of the simulation box. The lateral size of the box is set equal to the desired pitch, and periodic boundary conditions are used to simulate an infinite array. A broad-band (λ = 400 – 900 nm) plane wave is

launched from the top. Power monitors above the source and 50 nm below the Au-SiO_2 interface are used to monitor the reflection and transmission respectively. Since the gold is the only absorbing material in the simulation box, the absorption of the hole array is calculated as $1 - R - T$. The mesh size is set to 10 nm, with a 1.0-2.5 nm refinement mesh around the hole.

S9. Mechanism of Resonant Absorption in Hole Arrays

Resonant absorption of light in the hole arrays results from the diffractive coupling of incident light to surface plasmon polaritons (SPP) propagating at the metal-dielectric interface (*11, 30*). For the thin (18 nm) Au films used, SPPs on the Au-air and the Au-glass interface are strongly coupled (*31*), giving rise to symmetric and anti-symmetric insulator-metal-insulator (IMI) SPP modes. Figure S8A shows the calculated mode profile of the in-plane magnetic field component of the anti-symmetric mode for the glass-Au-air layer geometry at a free-space wavelength λ = 600 nm. In the calculations, optical constants for Au were taken from the Brendel and Bormann model (*13*), which show good correspondence with data from Johnson and Christy (*27*). The index of glass was taken as n = 1.46. The dispersion for the anti-symmetric IMI SPP is shown in Figure S8B. For comparison, the light line in air and the dispersion of single-interface SPPs on a semi-infinite Au substrate are also shown. As can be seen, the strong coupling of SPPs across the Au films leads to large wave vectors compared to the free-space or single-interface SPPs.

Figure S8C shows the propagation length of the IMI SPP as a function of wavelength. Data for a semi-infinite Au substrate are also shown. Clearly, the IMI mode has a strongly reduced propagation length due to the strong absorption in the metal (*31*), the latter obviously a desired feature to achieve a strong plasmoelectric effect.

Incident light can couple to the IMI SPPs through diffractive coupling via (±1,0), (0,±1), (±1, ±1) and higher order grating orders. To investigate which coupling order is dominant we performed FDTD simulations of the absorption in hole arrays (225 nm pitch) for angles of incidence $\theta = 0°$ and $\theta = 25°$ in a plane along the (0,1) axis of the array, for both s- and p-polarized light (data not shown). We find identical absorption spectra for the two angles for s-polarized light, whereas the spectra for p-polarized light differ significantly. From this we conclude that the in-plane component $k_0 \sin(\theta)$ of the incoming wave vector is orthogonal to k_{IMI}, which implies the incident light couples to the (0,±1) and (±1,0) orders. The peak resonance wavelengths λ_{res} for the absorption spectra simulated by FDTD for different array pitch (Λ, indicated in the figure) are plotted in Figure S8B as $2\pi/\lambda_{res}$, with the x-coordinate given by $2\pi/\Lambda$, corresponding to coupling through (±1,0) and (0,±1) orders (open circles). The data points lie quite close to the calculated dispersion curves indicating that absorption of incident light occurs through the (±1,0) and (0,±1) orders, with good agreement observed for the wavelength at which the experiments were done (λ = 600 - 700 nm, k_0 ~10 μm^{-1}). Note that the large discrepancy for 150 - 175 nm pitch can be attributed to a second branch of the dispersion curve as described in Ref. (*32-34*), a detailed discussion of which goes beyond the scope of this paper (*32, 33*).

The dispersion data in Figure S8B provide guidelines for the design of the array pitch in order to achieve efficient diffractive coupling from the normal-incident light beam to the in-plane IMI SPPs for a given incident wavelength. Due to the strong

dispersion, the array pitches required to couple to the IMI SPP are much smaller than the free-space wavelength (e.g. 200 nm at λ = 600 nm) (*30*).

Next, we calculated the effect of a variation of the electron density in the Au film on the IMI SPP dispersion. Variations in carrier density n were included in the optical constants for Au as described in section S1. Figure S8B shows the dispersion curves for electron densities in the range of $n = 0.9 \times n_{Au}$ (red) to $n = 1.1 \times n_{Au}$ (blue). A decrease in electron density redshifts the dispersion curve, analogous to what is observed for the localized resonances in the colloidal nanoparticles. In the spectral range where the resonant absorption occurs, a 1% change in electron density gives rise to a spectral shift of ~1.5 nm. This matches well with the spectral shift observed in the FDTD simulated absorption spectra for the different electron densities (not shown here). It is this dependence of the dispersion on the electron density, that in turn modifies the absorption efficiency, that is the driving mechanism for the plasmoelectric effect in the hole arrays.

Note that the absorption mechanism described here is very similar to the phenomenon of extraordinary transmission (EOT) in sub-wavelength hole arrays in optically thick films (*11, 35*), the only difference being that for EOT the SPPs on the air-Au and glass-Au interface do not couple, such that the SPP absorption losses are minimized rather than maximized, as is desired for the plasmoelectric effect (*31*).

S10. Spectral Broadening and Red-shift in Measured Spectra

Figure 4D shows that the wavelength of the zero-crossing in the KPFM spectrum is slightly blue-shifted with respect to the measured absorption maximum in Fig. 4C. This blueshift is more pronounced for hole arrays of smaller pitch. Based on the absorption mechanism described above, this discrepancy can readily be explained by the difference in numerical aperture (NA) of the objectives used for the two measurements. Transmission and reflection experiments were made using an NA=0.8, corresponding to a wide range of angles of incidence up to 53°. This gives rise to a large spread in the in-plane component of the wave vector of the incoming light, which translates into a large spread in spectral position along the dispersion curve. KPFM measurements were made using a lens with NA=0.25, giving rise to much sharper absorption peaks.

To quantify the effect of angular spread on the absorption spectra we performed FDTD simulations for a hole array (225 nm pitch), for different angles of incidence. Single-wavelength simulations were performed in the spectral range of λ = 500 – 700 nm, in steps of 5 nm. A plane-wave source was launched with an angle of incidence θ, p-polarized along one of the axis of the hole array. Bloch boundary conditions were used in the lateral direction of propagation.

Figure S9A shows the simulated absorption for $0° \leq \theta \leq 14°$ (blue to red), corresponding to the angles of incidence for NA=0.25 for the KPFM measurement. Also shown is the calculated absorption spectrum for normal incidence (solid black line) and the absorption averaged over all angles (dashed black line). Figure S9A shows only a small effect of angular spread for the NA=0.25 lens. Figure S9B shows the absorption spectra for an angular range ($0° \leq \theta \leq 53°$) corresponding to the NA=0.8 objective used in the transmission and reflection experiments. A pronounced redshift is observed for larger angles of incidence. Figures S9A,B also show the angle-averaged absorption spectrum, for the NA=0.8 geometry it shows a strong redshift compared to the absorption for normal incidence, as well as significant spectral broadening. The observation of a

redshifts indicates light couple to the (-1,0) order, consistent with what was observed by Braun et al. in absorption measurements on Au hole arrays (*31*). Note that to calculate a properly angle-weighted absorption spectrum the intensity profile on the back focal plane of the objective, and the transfer function of the objective must be taken into account. Nonetheless, the data in Figure S9 explain that the resonant absorption manifest in the KPFM signal in Fig. 4D is blueshifted and spectrally narrower compared with the measured absorption spectra in Fig. 4C. Finally, we note that for unpolarized light, variations in incident angle will lead to a further broadening of the absorption spectrum due to the different coupling conditions for different polarizations at different incident angles.

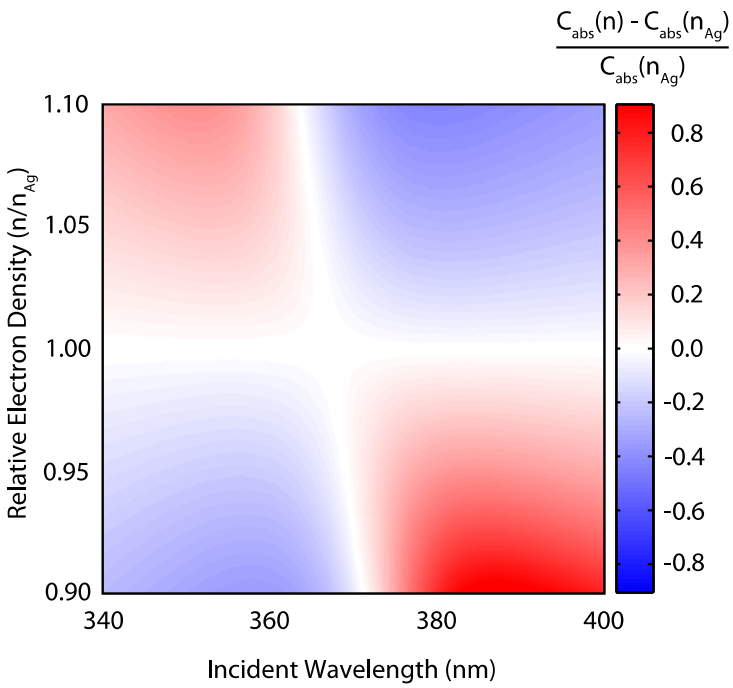

Fig. S1.

Relative change of the absorption cross section, $C_{abs}(n, \lambda)$, (color scale) of a 20-nm-diameter Ag nanoparticle in vacuum, as a function of wavelength and electron density, n, compared with the absorption cross section for a neutral Ag silver particle with electron density n_{Ag}.

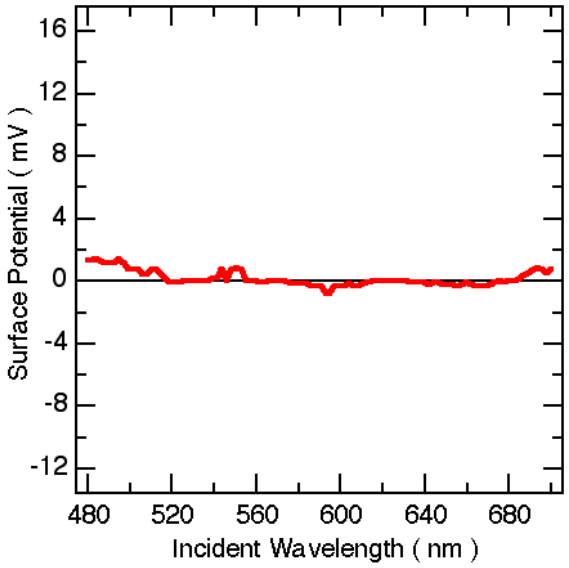

Fig. S2

KPFM-measured surface potential from a control experiment of bare ITO/glass under 1W/cm^2 scanned monochromatic illumination, plotted on the same scale as Fig. 2B.

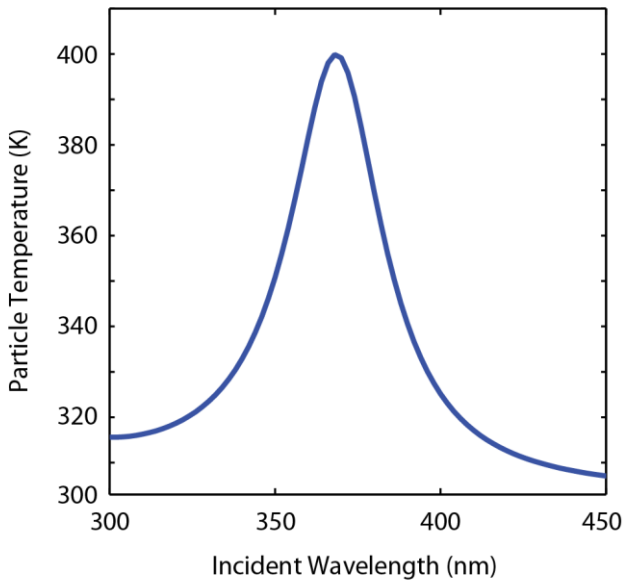

Fig. S3

Calculated temperature for a 20-nm-diameter Ag particle in vacuum as a function of illumination wavelength (1 mW/cm2).

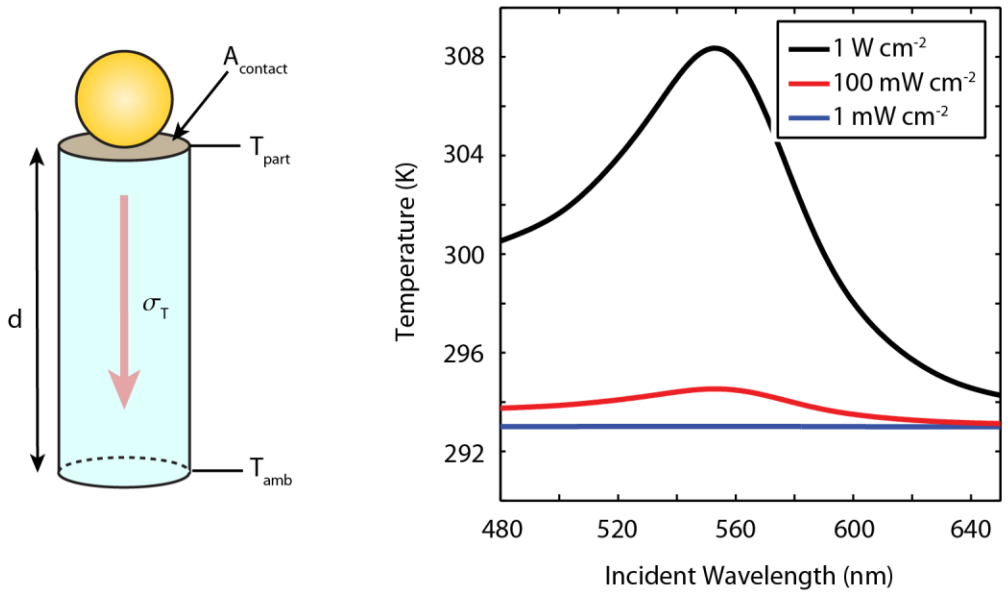

Fig. S4

(Left) Sketch of 1D heat diffusion model (left) for a Au nanoparticle on ITO/glass. (Right) Au nanoparticle temperature as a function of illumination wavelength, corresponding to the experiments in Fig. 2B.

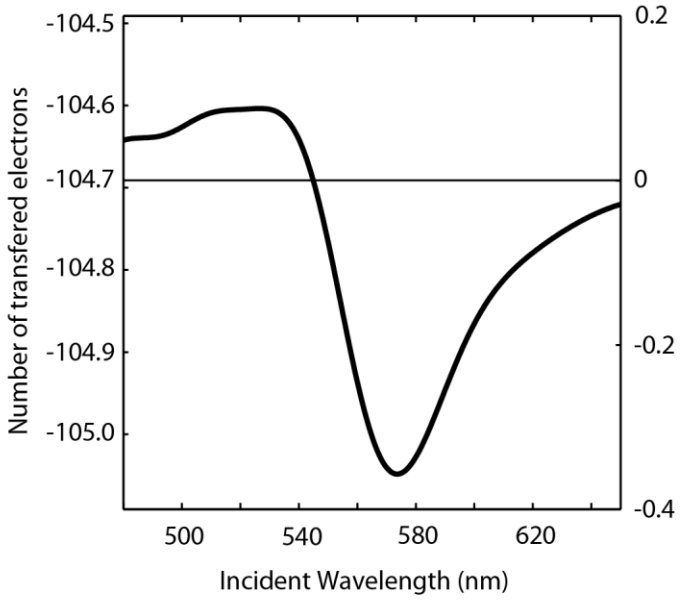

Fig. S5

Calculated excess electron number N-N_0 (left-hand scale) for a 60-nm-diameter Au particle on ITO/glass as a function of illumination wavelength (1000 mW/cm^2). The average number of electrons generating the plasmoelectric effect is shown by the right-hand scale.

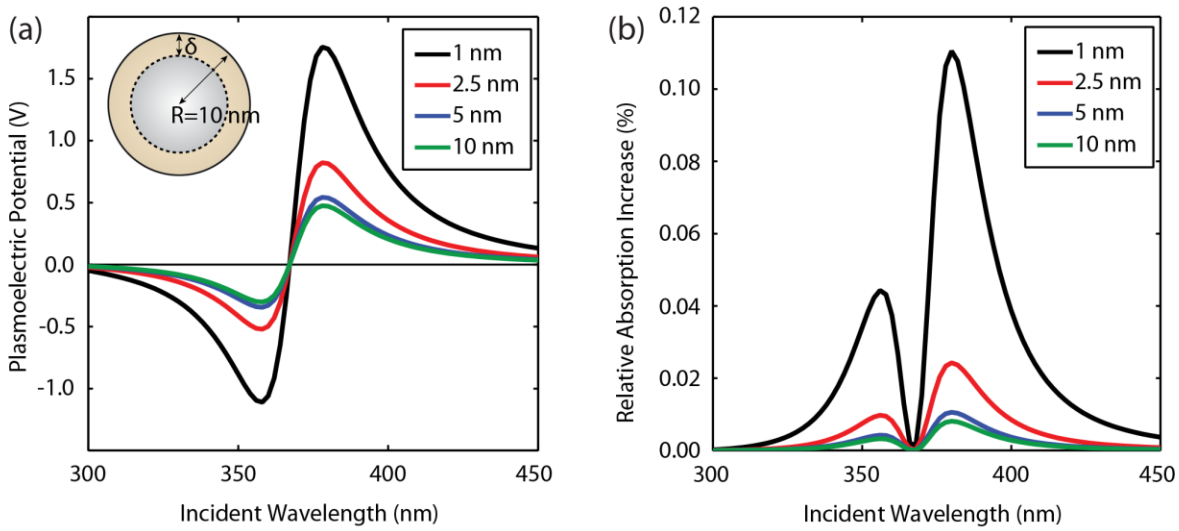

Fig. S6.

Calculated induced potential (A) and relative increase in absorption compared with a neutral particle (B) for a 20-nm-diameter Ag nanoparticle in vacuum as a function of illumination wavelength for shell thicknesses of 1.0, 2.5, 5.0 and 10 nm (black, red, blue and green trace respectively). The illumination power density is 10 mW cm^{-2}.

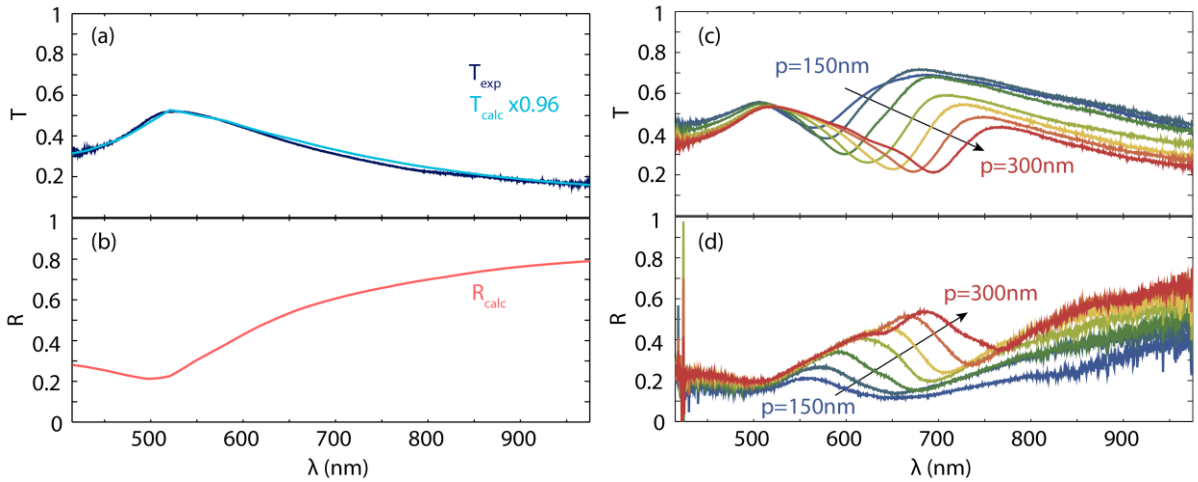

Fig. S7

(A) Measured (dark blue) and calculated (light blue) transmission spectrum for a 18 nm thick bare Au film on glass. (B) Calculated reflection spectrum for the same geometry. Measured transmission (C) and reflection spectra (D) of square arrays of 100 nm diameter holes in a Au film with pitch ranging from 150-300 nm, in 25 nm steps (blue to red).

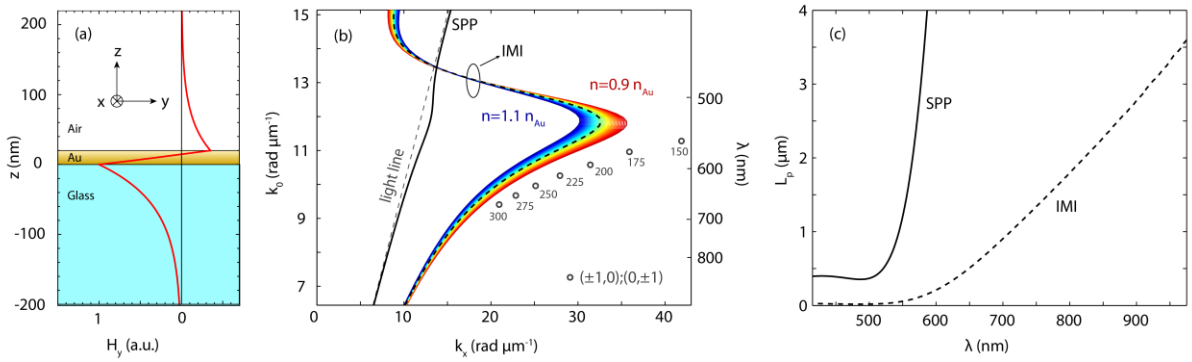

Fig. S8

(A) Field profile (in-plane magnetic field component) of the anti-symmetric IMI mode for a glass-Au-air layer geometry at a free-space wavelength λ = 600 nm. (B) Calculated dispersion for the anti-symmetric IMI SPP (black dashed line), and the SPP for a semi-infinite Au substrate (black solid line). Also shown is the light line in air (gray dashed). The colored lines show the calculated IMI dispersion curves for modified electron densities n in Au, ranging between 0.9-1.1 times the bulk density (red-blue). Also shown are the wavelengths of the peaks in the absorption spectra obtained from FDTD simulations plotted against wave vectors corresponding to (±1,0) and (0,±1) grating orders (open dots). The numbers next to the dots refer to the pitch (in nm) of the arrays for which these numbers were determined. (C) SPP intensity propagation length of the IMI (dashed line) SPP and of the SPP mode on a semi-infinite substrate (solid line).

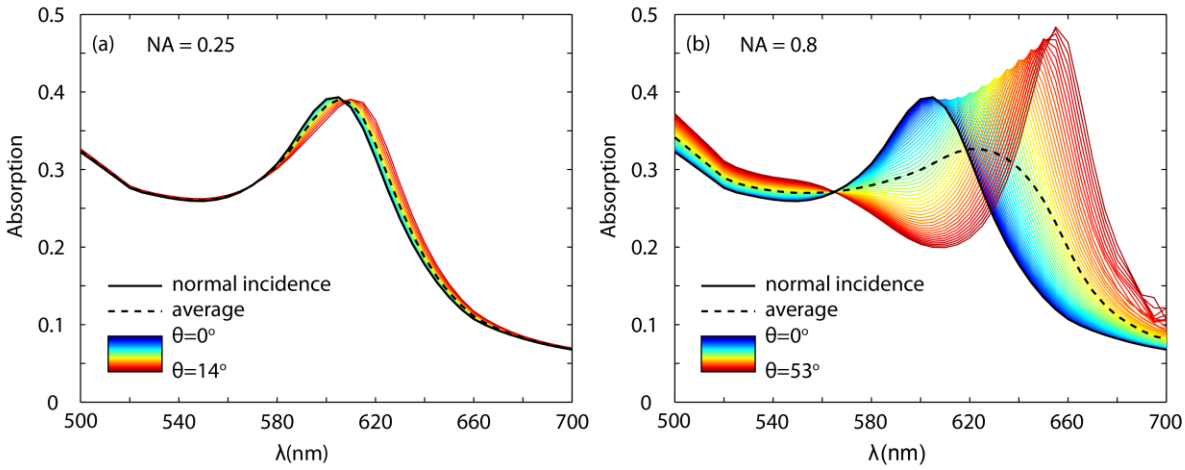

Fig. S9

Absorption spectra for a 225 nm pitched array, illuminated at different angles of incidence (colors) corresponding to the angles within the range of a NA=0.25 (A, used for KPFM measurements) and NA=0.8 (B, used for transmission and reflection experiments). A clear red-shift is observed for larger angles of incidence. The spectrum for normal incidence (solid black) and the average over all angles (dashed black) are also shown, clearly showing the effective redshift and broadening for the larger NA.